energies

MDPI

Article

Performance Comparison Between Microstepping and Field-Oriented Control for Hybrid Stepper Motors

Emilio Carfagna [1], Giovanni Migliazza [1], Marcello Medici [2] and Emilio Lorenzani [1,*]

[1] Department of Science and Methods for Engineering, University of Modena and Reggio Emilia, 42121 Reggio Emilia, Italy; emilio.carfagna@unimore.it (E.C.); giovanni.migliazza@unimore.it (G.M.)
[2] System Electronics, 41042 Fiorano Modenese, Italy; marcello.medici@systemelectronics.com
* Correspondence: emilio.lorenzani@unimore.it

Abstract: With their cost-effective manufacturing process, hybrid stepper motors (HSMs) are a popular choice for position control in low-power industrial applications. These versatile motors offer a compelling solution for reducing system costs and size since at standstill/low speeds, HSMs typically have higher torque density with respect to low-power permanent magnet (PM) motors. This higher torque density determines a reduced use of rare-earth PMs and, therefore, a lower environmental footprint. In practical applications, the commonly used microstepping control faces low efficiency, low dynamic performance, vibrations, and a variable maximum continuous torque depending on the working point. In this paper, the operating region of an HSM is extended in the field-weakening (FW) region, showing how field-oriented control (FOC) with FW allows one to strongly increase the drive performance with a slight cost increase thanks to the availability of low-cost magnetic encoders. Due to the fact that FOC provides only the requested current, the HSM faces lower temperatures, lower insulation degradation, and lower permanent magnet demagnetization issues. An experimental evaluation comparing the commonly used microstepping and the proposed FOC with FW is performed on four commercial HSMs with different DC voltage power supplies using an industrial test bench. In particular, the experimental campaign has a focus on steady-state conditions in the case of the maximum continuous torque, showing the advantages of FOC with FW because the advantages in transient conditions are well known.

Keywords: hybrid stepper motors; microstepping; field-oriented control; field-weakening region; speed range extension; maximum continuous torque

check for updates

Academic Editor: Chunhua Liu

Received: 11 December 2024
Revised: 9 January 2025
Accepted: 17 January 2025
Published: 24 January 2025

Citation: Carfagna, E.; Migliazza, G.; Medici, M.; Lorenzani, E. Performance Comparison Between Microstepping and Field-Oriented Control for Hybrid Stepper Motors. *Energies* **2025**, *18*, 553. https://doi.org/10.3390/en18030553

1. Introduction

High-pole-count machines such as direct-drive motors (or torque motors) [1] and hybrid stepper motors (HSMs) [2] are characterized by higher motor torque capacity with respect to machines with lower pole counts [3].

A hybrid stepper motor is used in incremental motion drives because, when powered, it locks itself in a very precise angular position. The rotation occurs through the passage of successive equilibrium positions. One of the key advantages of HSMs is their ability to be controlled in an open loop using input step pulses [4]. Stepper motors are widely utilized in a variety of low-power industrial applications as a cost-effective solution. They are capable of providing accurate positioning and high torque at low speeds thanks to their enhanced torque density [5] compared to traditional permanent magnet (PM) machines [6]. Such a motor's combination of low cost, high torque density, and positioning accuracy make it a popular choice for different medical, industrial, and consumer applications. Some examples of applications are (i) medical applications, such as micro-surgical manipulations [7–9], laboratory equipment for precise dosage control through pipettes [10], or exoskeletons to restore motion ability [11], (ii) robotic arms and grippers for industrial uses, where they can efficiently drive integrated drives to ensure high position accuracy [12–14], industrial equipment calibration [15], and sun tracking [16], (iii) consumer applications, including ink-jet printers and 3D printers [17,18], (iv) wireless applications that eliminate wires and the need for controllers and sensors on the secondary side [19], and (v) nuclear applications with long cables driving an axis of a large hadron collider (LHC) collimator [20,21] and a scintillator-based fast-ion loss detector (FILD) [22].

The applications mentioned above necessitate a robust actuator capable of withstanding vibrations while promptly and precisely responding to command signals and overcoming dynamic torque loads. However, due to motor inertia, the rotor tends to oscillate around the desired final position before stabilizing. Microstepping techniques can help achieve smoother behavior [23], but step losses due to unexpected load torque variations remain a concern. These step losses can be mitigated by supplying the stepper motor with a phase current higher than the minimum required. Yet, this approach leads to increased power losses [24]. In summary, the stepper motor's open-loop control capability is a significant benefit, but the challenges of rotor oscillation and step losses must be addressed through techniques such as microstepping and careful current control to ensure reliable performance in these demanding applications. Improved microstepping techniques that measure the rotor angle can be found in [25]; these techniques adjust the stator excitation angle and the current simultaneously on the basis of the feedback angle, while the authors of [26] use a variable-frequency controller based on a hyperbolic tangent function instead of the classical proportional–integral (PI) control method, and the authors of [27] combine the precision of PI and the robustness of sliding mode control with a weight adjustment based on the operating conditions.

The mathematical dq model of an HSM used for control design is the same as a surface-mounted PM synchronous machine (SPMSM), with additional no-idealities as high-cogging torque ripple [2,28]. In this scenario, field-oriented control (FOC) becomes a valid alternative that is able to maximize the performance [2]. Recent contributions with FOC where mechanical quantities (i.e., rotor position/speed) are measured can be found in [29], where the minimization of the cogging torque with a discrete-time synthesis is proposed, whereas the reader can refer to [30] for sensorless control (i.e., control that relies on the measured currents and on the reference voltages without measuring the rotor position/speed) of HSMs comparing the extended Kalman filter and the stator flux observer commonly used for synchronous machines.

A characteristic not yet exploited for HSMs is the higher capability for field weakening (FW) thanks to a short circuit current that is lower than the nominal one [31]. This characteristic is common in the case of machines with large winding inductance, and, consequently, using maximum torque per voltage (MTPV) control, an infinite constant-power speed ratio can be obtained [32–34]. Accurate knowledge of the rotor flux orientation is essential for the FOC of synchronous machines with permanent magnets. This orientation is typically measured using position sensors such as encoders or resolvers mounted on the machine's shaft. The performance of these sensors is crucial, as the position measurement directly impacts the quality of the torque produced by the machine [35]. It is important to note that even high-end, expensive sensors with high resolution, precision, and accuracy can exhibit position errors. These errors can arise from various factors, such as non-ideal mechanical installation [36] or interference from the system and environment, such as vibration and temperature, which can affect the measurement accuracy of optical and magnetic encoders [37,38]. With low-resolution encoders, proper techniques are used for the position and speed extraction [39].

The purpose of this study is the comparison between classical microstepping control and FOC enforced with FW control. To perform FOC, a low-cost magnetic encoder with 5000 ppr is adopted. A very deep experimental evaluation is performed on four commercial HSMs (with rated torques from 2 to 8 N m) and with different DC voltage power supplies using an industrial test bench to show the improvement in terms of efficiency, speed range extension, and torque capability in the field-weakening region.

This paper is organized as follows: Section 2 describes the adopted mathematical model of an HSM in the stationary (α, β) reference frame. Sections 3 and 4 report the implemented control strategies; in particular, classical microstepping is discussed in Section 3, with a focus on the mechanical resonance, whereas field-oriented control with field weakening is shown in Section 4. Section 5 verifies the strategies with an experimental test, followed by conclusions.

2. Hybrid Stepper Motor Model

The dynamic of a two-phase hybrid stepper motor in the stationary (α, β) reference frame under the assumption of sinusoidal flux distribution is given by [30]

$$\begin{cases} \dot{\theta} = \omega \\ J\dot{\omega} + F\omega = k_{\mathrm{M}}\Big(-i_\alpha \sin(N_r\theta) + i_\beta \cos(N_r\theta)\Big) - T_L - T_c \\ T_c = N_r F_m^2 \sum_{j=1}^{m} 4jP_{4j}\sin(4jN_r\theta) \\ u_\alpha = L_0\dfrac{di_\alpha}{dt} + R_s i_\alpha - k_{\mathrm{M}}\omega\sin(N_r\theta) \\ u_\beta = L_0\dfrac{di_\beta}{dt} + R_s i_\beta + k_{\mathrm{M}}\omega\cos(N_r\theta) \end{cases} \tag{1}$$

where θ is the (mechanical) rotor angle, ω is the (mechanical) rotor speed, (i_α, i_β) are the stator currents, and (u_α, u_β) are the stator voltages in the fixed (α, β) reference frame. The variables $(\theta, \omega, i_\alpha, i_\beta)$ are the state variables, while (u_α, u_β) are the control inputs, and the load torque T_L is the unknown disturbance input. The other model parameters are the viscous friction coefficient F, the number of rotor teeth N_r, the moment of inertia J, the stator winding resistance R_s, the stator inductance L_0, and the torque constant k_{M} equal to $N_r\Phi_{\mathrm{PM}}$, where Φ_{PM} is the flux linkage provided by the permanent magnet. The term T_c models the disturbance torque due to cogging (F_m is the magneto-motive force of the permanent magnet, and P_{4j} is the amplitude of the j harmonics [28]). The derivation of the model above is obtained under the assumptions that the self and mutual inductance of the two windings are constant with respect to θ.

3. Microstepping Control

Microstepping is reported in Figure 1, and it is usually employed to improve the motion stability and resolution of a hybrid stepper motor.

For two-phase HSMs in the control method, two sinusoidal inputs shifted by 90° are given for position tracking. The reference currents $i_\alpha^\star$ and $i_\beta^\star$ are given by

$$\begin{cases} i_\alpha^\star = I_{\mathrm{N}}\cos(N_r\theta^\star) \\ i_\beta^\star = I_{\mathrm{N}}\sin(N_r\theta^\star) \end{cases} \tag{2}$$

where I_N is the amplitude of the nominal current, and $\theta^\star$ is the desired position. Hysteresis controllers are used on the current loops. Microstepping control can be optimized by changing the hysteresis. If the hysteresis's window is larger, the average switching frequency on the devices is reduced at the cost of worst results on the regulation of the currents due to increased ripple. If the window is smaller, the regulation of the currents in the fixed reference frame is better at the cost of a higher switching frequency. The drive performance at high speed is affected by the increased back EMF, so the current-loop performance is dependent on the microstepping frequency. As noted by [40], when increasing the microstepping frequency, the current amplitudes decrease with the available torque.

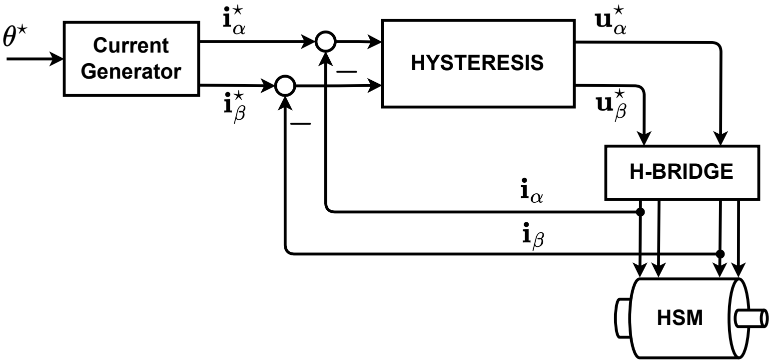

Figure 1. Classical microstepping with hysteresis control in the stationary (α, β) reference frame.

Mechanical Resonance

Furthermore, the HSM is subject to mechanical resonance, which significantly impacts its performance. The system's response to each single-step input is highly oscillatory in nature. This oscillatory behavior limits the operating speed of the HSM, as the system must settle within the required accuracy at each position before the next step can be executed. The natural frequency of rotor oscillation about the equilibrium position, denoted as f_n, is given by the following equation assuming an undamped system [41]:

$$f_n = \frac{1}{2\pi}\sqrt{\frac{k}{J}} \tag{3}$$

where k represents the stiffness of the torque–position characteristic, and J is the inertia contribution from the motor and load. A small amount of viscous friction is present, resulting in lightly damped oscillations. This means that the rotor will eventually settle at the equilibrium position, but not without passing through several cycles of oscillation. One significant consequence of the highly oscillatory single-step response is the occurrence of resonance effects at stepping rates up to the natural frequency of rotor oscillation, f_n. This resonant behavior of the system leads to a loss of motor torque at well-defined stepping rates. To address this issue, additional techniques and design considerations may be required. Further details on mitigating the effects of this mechanical resonance with open-loop control such as microstepping can be found in the referenced literature [41,42].

4. Field-Oriented Control with Field Weakening

Field-oriented control with a field-weakening strategy is reported in Figure 2. With respect to microstepping control, the use of an encoder is mandatory to measure the angle and the speed of the machine, causing a slight increase in the costs of the drive. Considering the stepper motor model in the stationary (α, β) reference frame in (1), the Park transformation is introduced; in this way, the vectors $u = [u_\alpha, u_\beta]^T$ and $i = [i_\alpha, i_\beta]^T$

in the stationary (α, β) frame are transformed into vectors expressed in the rotating (d, q) reference frame:

$$\begin{bmatrix} w_d \\ w_q \end{bmatrix} = \begin{bmatrix} \cos(N_r\theta) & \sin(N_r\theta) \\ -\sin(N_r\theta) & \cos(N_r\theta) \end{bmatrix} \begin{bmatrix} w_\alpha \\ w_\beta \end{bmatrix} \tag{4}$$

With the transformation introduced in (4), the dynamic of a two-phase hybrid stepper motor in the (d, q) reference frame, according to [2], is given by

$$\begin{cases} \dot{\theta} = \omega \\ J\dot{\omega} + F\omega = k_{\mathrm{M}} i_q - T_L - T_c \\ u_d = L_0 \dfrac{di_d}{dt} + R_s i_d - i_q N_r \omega L_0 \\ u_q = L_0 \dfrac{di_q}{dt} + R_s i_q + i_d N_r \omega L_0 + k_{\mathrm{M}}\omega \end{cases} \tag{5}$$

where (i_d, i_q) are the stator currents, and (u_d, u_q) are the stator voltages in rotating (d, q) reference frame. The variables $(\theta, \omega, i_d, i_q)$ are the state variables, while (u_d, u_q) are the control inputs. The term T_c has the same meaning as model (1).

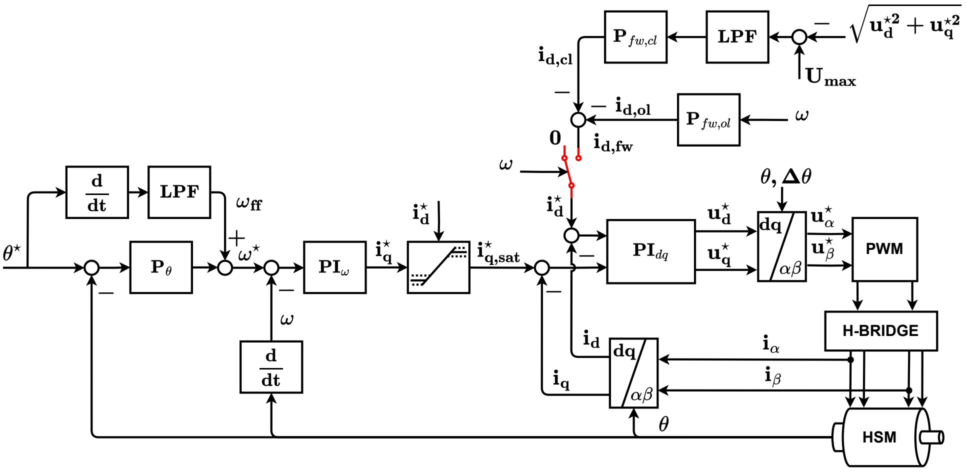

Figure 2. Field-oriented control with field-weakening control. The red switch uses FOC (with $i_d^\star$ equal to 0) or FOC with FW (with $i_d^\star$ equal to $i_{d,fw}$) depending on the measured speed.

The model in (5) is suitable for control design. The rotor speed dynamics in the (d, q)-coordinates are, as for DC machines, linear with respect to the stator current vector q-component i_q and can be controlled by it, with the stator current vector d-component i_d being freely assignable to match additional control requirements, such as the field-weakening control.

The classical field-weakening control based on output voltage regulation is avoided due the well-known problems of large sixth harmonic current, windup, and even instability problems [43,44]. In this study, the field-weakening control is implemented by adding an open-loop component and a closed-loop component. The open-loop component named $i_{d,ol}$ is considered equal to $K_{fw,ol}(\omega - \omega_{\mathrm{N}})/(\omega_{\max} - \omega_{\mathrm{N}})$, where $K_{fw,ol}$ is a proportional gain, ω_{N} is the base speed, and $\omega_{\max}$ is the maximum speed of the HSM. The closed-loop component is obtained by closing another loop on the error between the available voltage U_{max} and the demanded voltage module $\sqrt{u_d^{\star 2} + u_q^{\star 2}}$. This error is filtered by a first-order low-pass filter (LPF) and regulated with a proportional gain $K_{fw,cl}$. The result is the closed-loop current called $i_{d,cl}$. Summarizing, the field-weakening current $i_{d,fw}$ equal to $-i_{d,cl} - i_{d,ol}$ is

$$i_{d,fw} = -K_{fw,ol} \cdot \left(\frac{\omega - \omega_{\mathrm{N}}}{\omega_{\max} - \omega_{\mathrm{N}}} \right) - K_{fw,cl} \cdot \mathrm{LPF}\left(U_{max} - \sqrt{u_d^{\star 2} + u_q^{\star 2}} \right) \tag{6}$$

where the LPF has a form of the type $\omega_0/(s+\omega_0)$, ω_0 is the cutoff pulsation, and s is the Laplace operator. The classical FOC on the speed loop enforced with field-weakening control is designed as

$$\begin{cases} i_d^\star = \begin{cases} 0, & \text{for } \omega \le \omega_{\mathrm{N}} \\ i_{d,fw}, & \text{for } \omega > \omega_{\mathrm{N}} \end{cases} \\ i_q^\star = K_{p,s}\left(\omega^\star - \omega\right) + K_{i,s}\int_0^t \left(\omega^\star - \omega(\tau)\right) \mathrm{d}\tau \\ i_{q,sat}^\star = \begin{cases} \mathrm{sign}(i_q^\star)\sqrt{I_N^2 - i_d^{\star 2}}, & \text{for } |i_q^\star| \ge \sqrt{I_N^2 - i_d^{\star 2}} \\ i_q^\star, & \text{for } |i_q^\star| < \sqrt{I_N^2 - i_d^{\star 2}} \end{cases} \\ \begin{bmatrix} i_d \\ i_q \end{bmatrix} = \begin{bmatrix} \cos(N_r\theta) & \sin(N_r\theta) \\ -\sin(N_r\theta) & \cos(N_r\theta) \end{bmatrix} \begin{bmatrix} i_\alpha \\ i_\beta \end{bmatrix} \\ u_d^\star = K_{p,c}\left(i_d^\star - i_d\right) + K_{i,c}\int_0^t \left(i_d^\star - i_d(\tau)\right)\mathrm{d}\tau \\ u_q^\star = K_{p,c}\left(i_{q,sat}^\star - i_q\right) + K_{i,c}\int_0^t \left(i_{q,sat}^\star - i_q(\tau)\right)\mathrm{d}\tau \\ \Delta\theta = 1.5 T_s N_r \omega \\ \begin{bmatrix} u_\alpha^\star \\ u_\beta^\star \end{bmatrix} = \begin{bmatrix} \cos(N_r\theta + \Delta\theta) & -\sin(N_r\theta + \Delta\theta) \\ \sin(N_r\theta + \Delta\theta) & \cos(N_r\theta + \Delta\theta) \end{bmatrix} \begin{bmatrix} u_d^\star \\ u_q^\star \end{bmatrix} \end{cases} \tag{7}$$

The control depends on the positive control parameters $K_{p,c}$, $K_{i,c}$, $K_{fw,ol}$, $K_{fw,cl}$, $K_{p,s}$, and $K_{i,s}$. FOC is optimized using the Ziegler–Nichols method to find the values of the parameters for every control loop. The strategy imposes the currents $i_d^\star$ with respect to the voltage error and to the speed and $i_q^\star$ with respect to the desired torque; then, the current loops are closed considering the measured currents i_d and i_q. The output reference voltages $u_d^\star$ and $u_q^\star$ are transformed into the stationary (α, β) reference frame and applied to the machine. The value of $i_q^\star$ is subject to a variable saturation given by $i_d^\star$. When the HSM is outside the FW region, $i_d^\star$ is equal to zero, and the maximum value of $i_q^\star$ is the nominal current I_{N}. Otherwise, in FW region, $i_d^\star$ is different from zero, and the maximum allowed current $i_q^\star$ is saturated by $\sqrt{I_{\mathrm{N}}^2 - i_d^{\star 2}}$.

Following the volt–second principle in [2], the relationship between the actual voltage and the original voltage output by the current regulator is delayed by 1.5 T_s due to the pulse width modulation (PWM) delay. According to this consideration, the term $\Delta\theta$ in (7) is the rotor position compensation that adds $\Delta\theta$ to the electrical rotor angle $N_r\theta$ to take into account this delay. This compensation cannot be neglected in the high-speed region; for the motor under test, N_r is equal to 50, and the sampling period T_s is equal to 40 µs; as a consequence, $\Delta\theta$ is equal to 33.73° considering the maximum speed of 314 rad/s. To allow position control on $\theta^\star$, the strategy in (7) is designed as

$$\begin{cases} \omega_{\mathrm{FF}} = \mathrm{LPF}\left(\frac{d}{dt}\theta^\star\right) \\ \omega^\star = K_{p,\theta}\left(\theta^\star - \theta\right) + \omega_{\mathrm{FF}} \end{cases} \tag{8}$$

with the positive control parameter $K_{p,\theta}$ and the cut-off pulsation ω_0 of the LPF in the feedforward computation ω_{FF}.

5. Experimental Results

The aforementioned HSMs are installed on a test bench (see Figure 3) comprising an induction machine as a brake, as well as a torque transducer. The control schemes in Figures 1 and 2 were finally tested in experiments. The controllers were implemented in their discrete version on a commercial STM32H743ZI DSP controller, running at a sampling frequency of 40 kHz. The DSP was used to implement the proposed controls, as well as to generate the PWM signals and to acquire the two motor phase currents. A commercial programmable logic controller (PLC) manufactured by Beckhoff was used to compute the position/speed references and communicate with the DSP. The hybrid stepper motors are two-phase salient stepper motor (manufactured by System Electronics, Fiorano Modenese, Italy) with the NEMA34 standard, 50 rotor teeth, and a step angle of 1.8°, employing an incremental magnetic encoder with 5000 ppr; see Table 1 for further details. Stepper 1 and Stepper 2 had similar values, and the only visible difference was the weight of the HSMs, whereas Stepper 3 and Stepper 4 were smaller. In the following, the results with different values of DC-link voltage V_{DC} are reported.

Table 1. Stepper motors' nameplate parameters.

Parameter		**Stepper 1**	**Stepper 2**	**Stepper 3**	**Stepper 4**
Nominal phase current	I_N [A_{pk}]	10	10	9	9
Rotor teeth	N_r [Adim.]	50	50	50	50
Stator resistance	R_s [Ω]	0.23	0.22	0.16	0.12
Stator inductance	L_0 [mH]	2.3	2.3	1.5	0.85
Torque constant	k_M [Nm/A]	0.8	0.74	0.51	0.25
Nominal torque	T_L [N m]	7.2	6.5	4.2	2.1
Nominal speed (with V_{DC} of 70 V)	ω_N [rad/s]	30	35	50	100
Maximum speed	ω_{max} [rad/s]	314	314	314	314
Weight	M [kg]	5.2	4.2	3	2

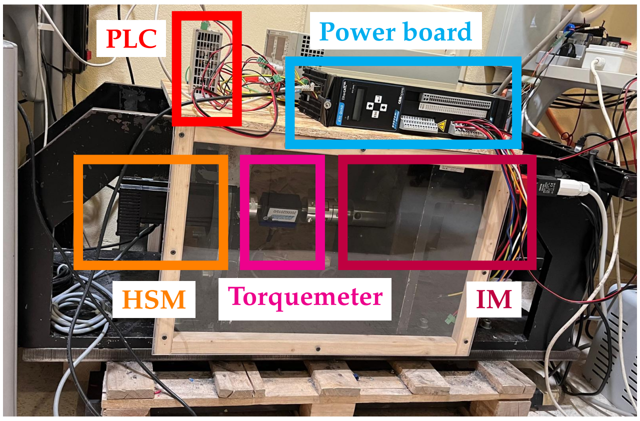

Figure 3. Test bench with HSM (Stepper 1, orange box), power board (cyan box), PLC (red box), torquemeter (magenta box) and induction machine as brake (IM, purple box).

5.1. Results with V_{DC} Equal to 70 V

Stepper 1 is considered as the reference machine. The results with different speed/torque working conditions are reported for microstepping control and FOC with FW using a DC-link voltage of 70 V.

Figure 4 reports the results in the low-speed region with a speed reference of 3.5 rad/s. It is worth noting that microstepping exhibits the steps (in particular, the full step is digitized in eight micro-steps) given by the control, while FOC has a smooth and continuous behavior. Furthermore, FOC applies only the requested current, whereas microstepping gives the maximum current in every operating condition.

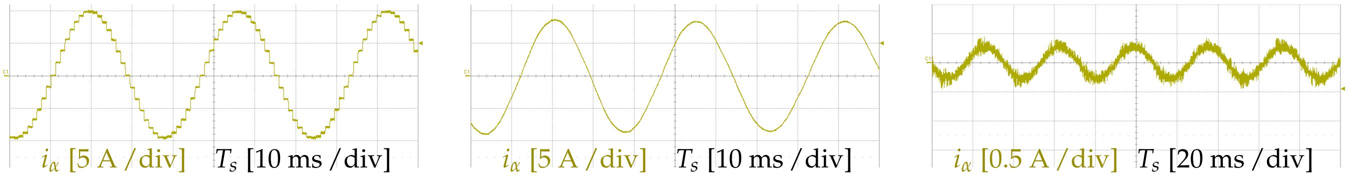

(**a**) (**b**) (**c**)

Figure 4. Stepper 1: Steady-state output current with microstepping control and FOC at ω = 3.5 rad / s with V_{DC} of 70 V. (**a**) Microstepping control with load torque of 7 N m. (**b**) FOC with load torque of 7 N m. (**c**) FOC at no-load.

When the HSM enters the field weakening region, the results are displayed in Figure 5 with a speed reference of 70 rad / s at no load. It can be seen that the microstepping in Figure 5a applies the maximum current even without load torque and the measured output current has a strong distortion, while the FOC with FW in Figure 5b has a sinusoidal output current with a lower peak because only the current required by FW is used. In fact, the root mean square (RMS) of the output current is 2.02 A_{RMS} for microstepping and 1.24 A_{RMS} for FOC with FW.

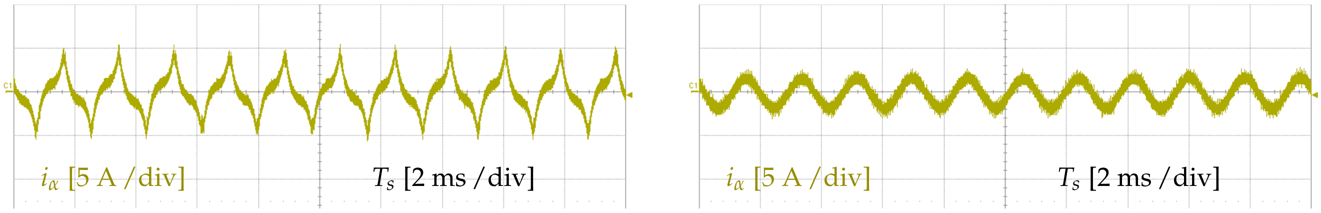

(**a**) (**b**)

Figure 5. Stepper 1: Steady-state output current with microstepping control and FOC at ω = 70 rad / s at no load with V_{DC} of 70 V. (**a**) Microstepping control at no load, I_{RMS} = 2.02 A_{RMS}. (**b**) FOC with FW at no load, I_{RMS} = 1.24 A_{RMS}.

Imposing a speed reference of 174 rad / s in Figure 6, it can be noted that microstepping presents a strong distortion, and it is not possible to apply the load torque; otherwise, the step will be lost. FOC with FW maintains a sinusoidal shape of the output current, and it is possible to apply a small load torque.

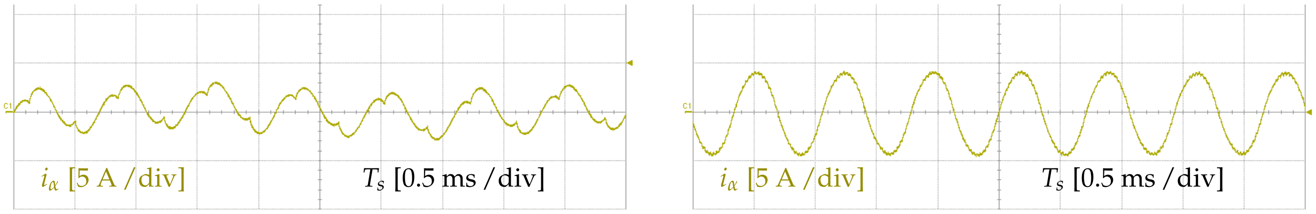

(**a**) (**b**)

Figure 6. Stepper 1: Steady-state output current with microstepping control and FOC at n = 174 rad / s with V_{DC} of 70 V. (**a**) Microstepping control at no load. (**b**) FOC with FW with load torque of 0.6 N m.

From the torque / speed characteristic displayed in Figure 7, it can be seen that FOC with FW is able to reach higher speeds, extending the speed range of the machine with respect to classical microstepping. Furthermore, the measured torque of FOC with FW is higher in every working condition. Figure 8 summarizes the waveform of the dq currents with a speed step starting from a standstill and reaching the maximum speed of 314 rad/s at no load with V_{DC} of 70 V. The minimum i_d current is limited to -4 A. At the beginning of the transient, the positive values of i_d are due to the absence of the decoupling between d and q axis.

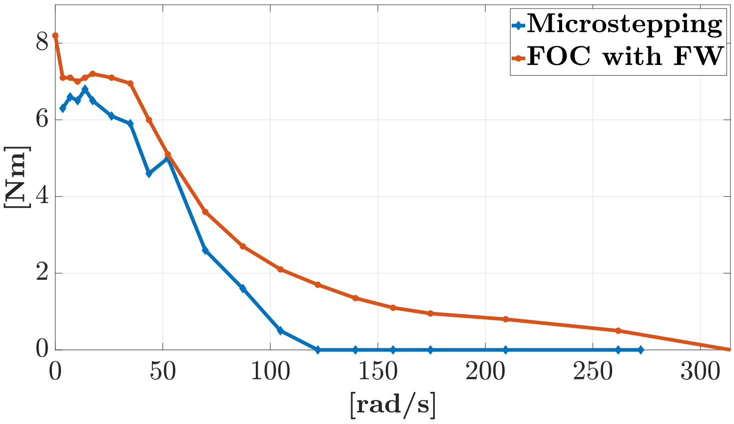

Figure 7. Stepper 1: Torque/speed characteristics with V_{DC} of 70 V with microstepping and FOC with FW.

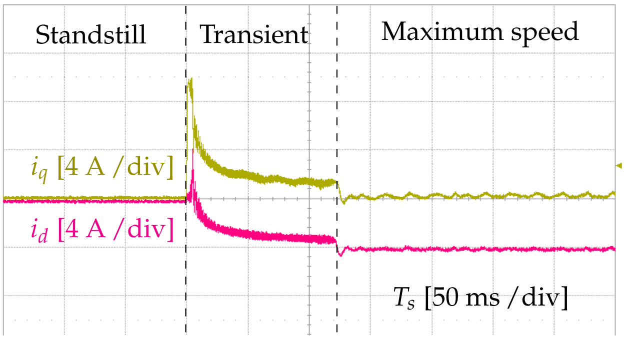

Figure 8. Waveform of the dq currents with a speed step from standstill to 314 rad/s at no load with V_{DC} of 70 V.

5.2. Results with V_{DC} Equal to 140 V

Stepper 1 is considered again as the reference machine. The results with different speed/torque working conditions are reported for microstepping control and FOC with FW using a DC-link voltage of 140 V.

Figure 9 reports the results in field-weakening region with a speed reference of 122 rad/s and a load torque of 4.5 N m. It is worth noting that microstepping exhibits distortion in the output current, while FOC has a smooth behavior by applying only the requested i_q to generate the electromagnetic torque and only the requested i_d to reach the FW region.

In Figure 10, the torque/speed curve is reported for every stepper motor considering V_{DC} of 140 V for microstepping control and FOC with FW. It can be seen that using FOC with FW, the torque remains constant until the nominal speed is reached, and then the torque profile decreases, while with microstepping the torque profile has different dips caused by the mechanical resonance, as discussed in Section 3. As already put in evidence by the previous subsection, the speed range is extended with FOC with FW.

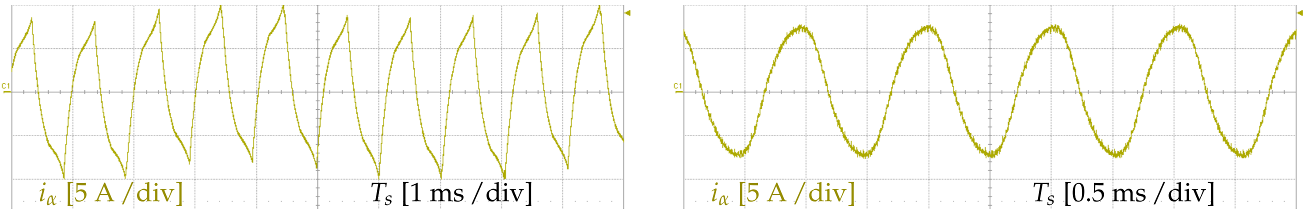

(**a**) (**b**)

Figure 9. Stepper 1: Steady-state output current with microstepping control and FOC at ω = 122 rad/s with V_{DC} of 140 V. (**a**) Microstepping control with a load torque of 4.5 N m. (**b**) FOC with FW with a load torque of 4.5 N m.

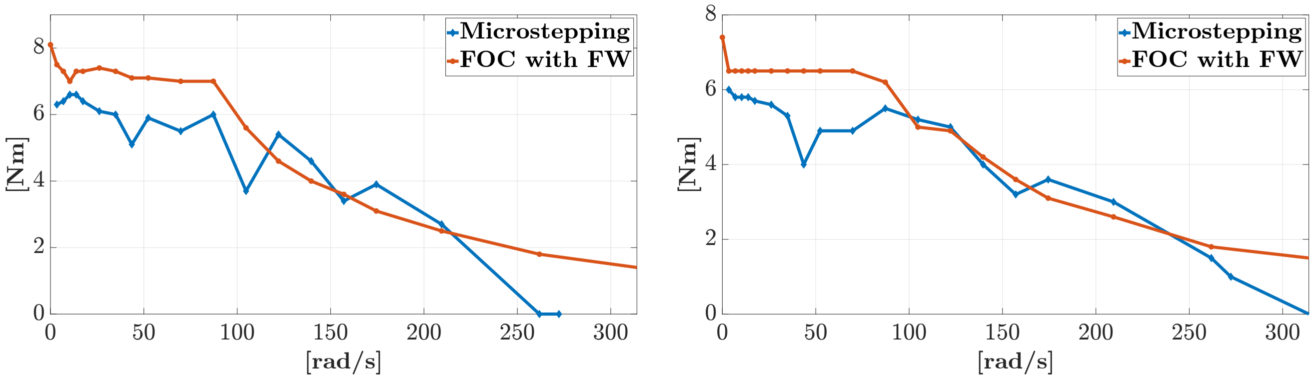

(**a**) Stepper 1. (**b**) Stepper 2.

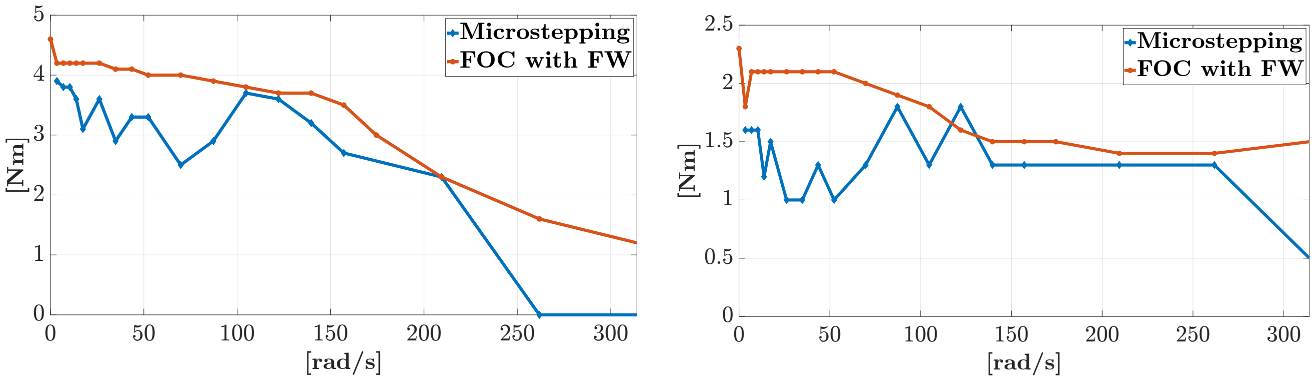

(**c**) Stepper 3. (**d**) Stepper 4.

Figure 10. Torque/speed characteristics of every HSM with V_{DC} of 140 V with microstepping and FOC with FW.

5.3. Results with V_{DC} *Equal to 48* V

The torque/speed curve is reported for every stepper motor in Figure 11 considering V_{DC} of 48 V for microstepping control and FOC with FW. The behavior of the torque/speed curve is the same as that seen with bigger values of V_{DC}. The region with constant torque is reduced to a smaller DC bus voltage, and the FW region is reached with lower speeds.

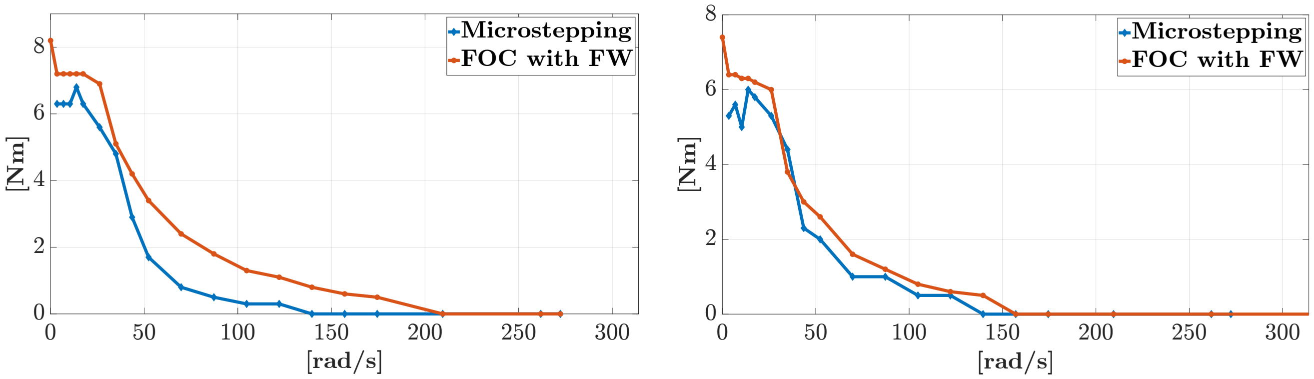

(**a**) Stepper 1. (**b**) Stepper 2.

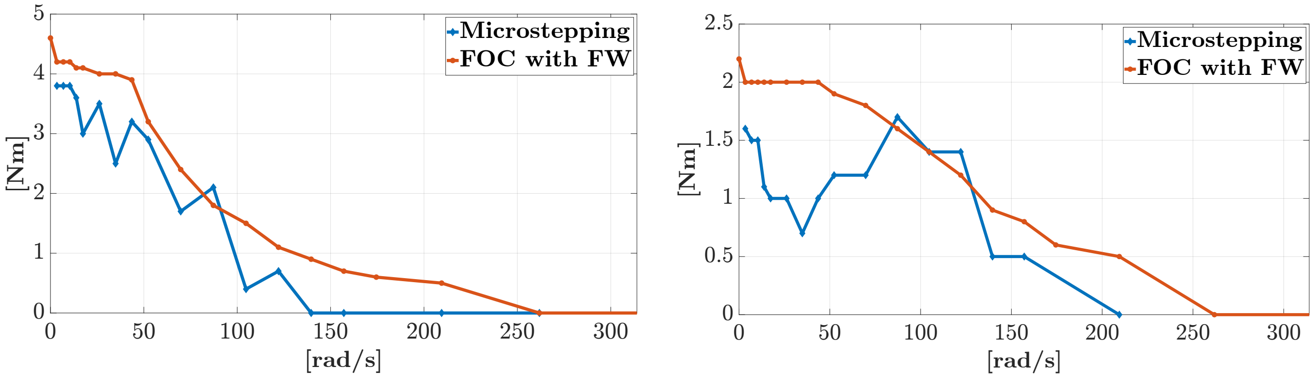

(**c**) Stepper 3. (**d**) Stepper 4.

Figure 11. Torque/speed characteristics of every HSM with V_{DC} of 48 V with microstepping and FOC with FW.

6. Conclusions

In this paper, a comparison between the commonly used microstepping control for HSM and a robust FOC with an FW strategy is carried out using an industrial test bench with different DC voltages with a particular focus on the behavior in high-speed regions. Microstepping has the advantage of controlling the HSM in an easy way, dividing the steps into smaller steps, but the strategy faces low efficiency and the possibility of losing the step due to mechanical resonance. For these reasons, FOC with an FW strategy is implemented to extend the speed range of the machine, obtain a smooth torque/speed curve, and reduce the power losses because only the requested current is provided. It is well known that FOC exhibits lower losses in practical applications and increased dynamic performances with respect to microstepping control. The speed range extension is relevant with lower DC bus voltage. For example, with 48 V, it can be seen that FOC with FW can provide torque with higher speeds. Considering Stepper 3 as a reference, FOC with FW can provide torque until 260 rad/s, while microstepping can work only in no-load conditions starting from 140 rad/s and starts to lose the step after 260 rad/s.

For these reasons, the comparison is mainly performed in steady-state condition with the application of the maximum continuous torque from a standstill to the maximum allowed speed. It is worth noting that FOC with FW is able to extend the speed range of the machine and provide higher torques. Additional experiments are added to show the smooth waveform of the *dq* currents during a speed step from a standstill to the maximum speed.

Author Contributions: Conceptualization, E.L. and M.M.; methodology, E.L. and E.C.; software, E.C., G.M. and M.M.; validation, E.C., G.M. and M.M.; investigation, E.C., G.M. and M.M.; data curation, E.C.; writing—original draft preparation, E.C. and E.L.; writing—review and editing, E.C. and E.L.; supervision, E.L. All authors have read and agreed to the published version of the manuscript.

Funding: This work was partially supported by the ESF REACT-EU: Programma Operativo Nazionale (PON) "Ricerca e Innovazione" 2014–2020, CCI2014IT16M20P005, Progetti DM 1062 dated 10 August 2021 and by the National Recovery and Resilience Plan (NRRP), Mission 04 Component 2 Investment 1.5—NextGenerationEU, Call for tender n. 3277 dated 30/12/2021. Award Number: 0001052 dated 23 June 2022.

Data Availability Statement: The original contributions presented in this study are included in the article. Further inquiries can be directed to the corresponding author.

Conflicts of Interest: Author Marcello Medici was employed by the company System Electronics. The remaining authors declare that the research was conducted in the absence of any commercial or financial relationships that could be construed as a potential conflict of interest.

References

1. Chung, S.U.; Moon, S.H.; Kim, D.J.; Kim, J.M. Development of a 20-pole–24-slot SPMSM with consequent pole rotor for in-wheel direct drive. *IEEE Trans. Ind. Electron.* **2016**, *63*, 302–309. [CrossRef]
2. Bernardi, F.; Carfagna, E.; Migliazza, G.; Buticchi, G.; Immovilli, F.; Lorenzani, E. Performance analysis of current control strategies for hybrid stepper motors. *IEEE Open J. Ind. Electron. Soc.* **2022**, *3*, 460–472. [CrossRef]
3. Taran, N.; Rallabandi, V.; Heins, G.; Ionel, D.M. Systematically exploring the effects of pole count on the performance and cost limits of ultrahigh efficiency fractional hp axial flux PM machines. *IEEE Trans. Ind. Appl.* **2020**, *56*, 117–127. [CrossRef]
4. Chen, Z.; Gao, X.; Wang, A.; Liang, Z.; Zhang, X. An online open-loop S-curve velocity profile control method for stepping motors on FPGA. *IEEE Trans. Ind. Electron.* **2024**, *71*, 16452–16462. [CrossRef]
5. Hojati, M.; Baktash, A. Design and fabrication of a new hybrid stepper motor with significant improvements in torque density. *Eng. Sci. Technol. Int. J.* **2021**, *24*, 1116–1122. [CrossRef]
6. Derammelaere, S.; Haemers, M.; De Viaene, J.; Verbelen, F.; Stockman, K. A quantitative comparison between BLDC, PMSM, brushed DC and stepping motor technologies. In Proceedings of the 2016 19th International Conference on Electrical Machines and Systems (ICEMS), Chiba, Japan, 13–16 November 2016; pp. 1–5.
7. Özelçi, E.; Etesami, E.; Rohde, L.A.; Oates, A.C.; Sakar, M.S. A robotic surgery platform for automated tissue micromanipulation in zebrafish embryos. *IEEE Robot. Autom. Lett.* **2024**, *9*, 327–334. [CrossRef]
8. Lenssen, T.; Dankelman, J.; Horeman, T. The SATA-drive: A modular robotic drive for reusable steerable laparoscopic instruments. *IEEE Trans. Med. Robot. Bionics* **2024**, *6*, 146–152. [CrossRef]
9. Zhang, Y.; Meng, M.Q.H.; Liu, L. Design and control of a compact electromagnetically driven laser scanner for robotic-assisted endoscopic microsurgeries. *IEEE Trans. Autom. Sci. Eng.* **2023**, *21*, 5997–6010. [CrossRef]
10. Sun, M.; Yao, Y.; Zhao, X.; Li, L.; Gong, H.; Qiu, J.; Liu, Y.; Zhao, X. Precise aspiration and positioning control based on dynamic model inside and outside the micropipette. *IEEE Trans. Autom. Sci. Eng.* **2023**, *20*, 385–393. [CrossRef]
11. Wang, T.; Song, Z.; Wen, H.; Liu, C. Lower extremity exoskeleton for human spinal cord injury: A comprehensive review. *IEEE Open J. Ind. Electron. Soc.* **2024**, *5*, 575–595. [CrossRef]
12. Wu, Z.; Yao, Y.; Liang, J.; Jiang, F.; Chen, S.; Zhang, S.; Yan, X. Digital twin-driven 3-D position information mutuality and positioning error compensation for robotic arm. *IEEE Sensors J.* **2023**, *23*, 27508–27516. [CrossRef]
13. Groenhuis, V.; Rolff, G.; Bosman, K.; Abelmann, L.; Stramigioli, S. Multi-axis electric stepper motor. *IEEE Robot. Autom. Lett.* **2021**, *6*, 7201–7208. [CrossRef]
14. Yeh, P.C.; Tsai, Y.S.; Lan, C.C. A compliant gripper with two-dimensional force sensing on each finger. *IEEE/ASME Trans. Mechatronics* **2024**, *29*, 1041–1051. [CrossRef]
15. Evangelidis, A.; Dimitriou, N.; Charalampous, P.; Mastos, T.D.; Tzovaras, D. Efficient deep Q-learning for industrial equipment calibration in elevator manufacturing. *IEEE Trans. Ind. Inform.* **2024**, *20*, 12220–12230. [CrossRef]
16. Fathabadi, H. Novel online sensorless dual-axis sun tracker. *IEEE/ASME Trans. Mechatronics* **2017**, *22*, 321–328. [CrossRef]
17. Nguyen, N.D.; Ashraf, I.; Kim, W. Compact model for 3D printer energy estimation and practical energy-saving strategy. *Electronics* **2021**, *10*, 483. [CrossRef]
18. Chou, C.H.; Duan, M.; Okwudire, C.E. A physics-guided data-driven feedforward tracking controller for systems with unmodeled dynamics—Applied to 3D printing. *IEEE Access* **2023**, *11*, 14563–14574. [CrossRef]

19. Li, S.; Chau, K.T.; Liu, W.; Liu, C.; Lee, C.K. Design and control of wireless hybrid stepper motor system. *IEEE Trans. Power Electron.* **2024**, *39*, 10518–10531. [CrossRef]
20. Masi, A.; Butcher, M.; Losito, R.; Picatoste, R. DSP based smart sensorless stepping motor driver for LHC collimators. *IEEE Trans. Nucl. Sci.* **2013**, *60*, 3514–3520. [CrossRef]
21. Masi, A.; Butcher, M.; Martino, M.; Picatoste, R. An application of the extended Kalman filter for a sensorless stepper motor drive working with long cables. *IEEE Trans. Ind. Electron.* **2012**, *59*, 4217–4225. [CrossRef]
22. Rivero-Rodriguez, J.F.; Velarde, L.; Williams, T.; Galdón-Quiroga, J.; García-Muñoz, M.; McClements, K.G. Initial operation of the scintillator-based fast-ion loss detector rotary and reciprocating system in MAST-U. *IEEE Trans. Plasma Sci.* **2024**, *52*, 3878–3884. [CrossRef]
23. Pillans, J. Reducing position errors by vibration optimization of stepper motor drive waveforms. *IEEE Trans. Ind. Electron.* **2021**, *68*, 5176–5183. [CrossRef]
24. Derammelaere, S.; Vervisch, B.; De Belie, F.; Vanwalleghem, B.; Cottyn, J.; Cox, P.; Van den Abeele, G.; Stockman, K.; Vandevelde, L. The efficiency of hybrid stepping motors: Analyzing the impact of control algorithms. *IEEE Ind. Appl. Mag.* **2014**, *20*, 50–60. [CrossRef]
25. Jiang, S.B.; Chuang, H.C.; Kung, C.W.; Deng, X.G.; Shen, Y.P.; Chen, L.W. Innovative microstepping motor controller with excitation angle-current dual-loop feedback control. *IEEE Access* **2023**, *11*, 62382–62393. [CrossRef]
26. Zhou, W.; Li, X.; Qian, J.; Xia, M.; Pu, Y.; Jiang, P.; Huang, J. Frequency modulation based on hyperbolic tangent function for position closed loop control of stepper motor. *IEEE Access* **2023**, *11*, 65066–65074. [CrossRef]
27. Lixian, S.; Rahiman, W. A compound control for hybrid stepper motor based on PI and sliding mode control. *IEEE Access* **2024**, *12*, 163536–163550. [CrossRef]
28. Matsui, N.; Nakamura, M.; Kosaka, T. Instantaneous torque analysis of hybrid stepping motor. *IEEE Trans. Ind. Appl.* **1996**, *32*, 1176–1182. [CrossRef]
29. Arias, A.; Caum, J.; Ibarra, E.; Griñó, R. Reducing the cogging torque effects in hybrid stepper machines by means of resonant controllers. *IEEE Trans. Ind. Electron.* **2019**, *66*, 2603–2612. [CrossRef]
30. Carfagna, E.; Migliazza, G.; Immovilli, F.; Verrelli, C.M.; Lorenzani, E. PMSM-model-based sensorless control of hybrid stepper motors: Performance and robustness to parameters dispersion. In Proceedings of the IECON 2020 The 46th Annual Conference of the IEEE Industrial Electronics Society, Singapore, 18–21 October 2020; pp. 1063–1068. [CrossRef]
31. EL-Refaie, A.; Jahns, T. Optimal flux weakening in surface PM machines using fractional-slot concentrated windings. *IEEE Trans. Ind. Appl.* **2005**, *41*, 790–800. [CrossRef]
32. Liu, H.; Zhu, Z.Q.; Mohamed, E.; Fu, Y.; Qi, X. Flux-weakening control of nonsalient pole PMSM having large winding inductance, accounting for resistive voltage drop and inverter nonlinearities. *IEEE Trans. Power Electron.* **2012**, *27*, 942–952. [CrossRef]
33. Miguel-Espinar, C.; Heredero-Peris, D.; Gross, G.; Llonch-Masachs, M.; Montesinos-Miracle, D. Maximum torque per voltage flux-weakening strategy with speed limiter for PMSM drives. *IEEE Trans. Ind. Electron.* **2021**, *68*, 9254–9264. [CrossRef]
34. Verrelli, C.M.; Carfagna, E.; Frigieri, M.; Crinto, A.S.; Lorenzani, E. A new Bernard–Praly-like observer for sensorless IPMSMs. *Automatica* **2022**, *140*, 110266. [CrossRef]
35. Lara, J.; Xu, J.; Chandra, A. Effects of rotor position error in the performance of field-oriented-controlled PMSM drives for electric vehicle traction applications. *IEEE Trans. Ind. Electron.* **2016**, *63*, 4738–4751. [CrossRef]
36. Lara, J.; Xu, J.; Chandra, A. A novel algorithm based on polynomial approximations for an efficient error compensation of magnetic analog encoders in PMSMs for EVs. *IEEE Trans. Ind. Electron.* **2016**, *63*, 3377–3388. [CrossRef]
37. Li, W.; Cai, N.; Ning, Z.; Dong, Y.; Wang, H. Error compensation for optical encoder via local-sinusoidal-assisted empirical mode decomposition with an optimization scheme. *IEEE Trans. Ind. Electron.* **2022**, *69*, 9596–9604. [CrossRef]
38. Chuang, H.C.; Kung, C.W.; Chen, L.W.; Jiang, S.B. Nonlinear error correction for magnetic encoders. *IEEE Sensors J.* **2023**, *23*, 9129–9135. [CrossRef]
39. Scelba, G.; De Donato, G.; Elsman, A.A.M.; Tornello, L.D.; Scarcella, G.; Capponi, F.G. Resolution of rotor position measurement: Modeling and impact on speed estimation. *IEEE J. Emerg. Sel. Top. Power Electron.* **2022**, *10*, 1992–2004. [CrossRef]
40. Bellini, A.; Concari, C.; Franceschini, G.; Toscani, A. Mixed-mode PWM for high-performance stepping motors. *IEEE Trans. Ind. Electron.* **2007**, *54*, 3167–3177. [CrossRef]
41. Acarnley, P. *Stepping Motors: A Guide to Theory and Practice*; IEE Control Engineering Series; Institution of Electrical Engineers:, London, UK, 2002.
42. Senjyu, T.; Uezato, K. Stability analysis and suppression control of rotor oscillation for stepping motors by Lyapunov's direct method. *IEEE Trans. Power Electron.* **1995**, *10*, 333–339. [CrossRef]

43. Kwon, T.S.; Sul, S.K. Novel antiwindup of a current regulator of a surface-mounted permanent-magnet motor for flux-weakening control. *IEEE Trans. Ind. Appl.* **2006**, *42*, 1293–1300. [CrossRef]
44. Kwon, Y.C.; Kim, S.; Sul, S.K. Voltage feedback current control scheme for improved transient performance of permanent magnet synchronous machine drives. *IEEE Trans. Ind. Electron.* **2012**, *59*, 3373–3382. [CrossRef]